Simultaneous H$_2$ fuel evolution and value-added organic transformation from a one-dimensional noble-metal-free photocatalyst with spatially separated catalytic sites

Yuexing Chen [a,b], Hui Xie [a], Ming Ma [c], Zheng Xing [a,*]

[a] School of Chemical Engineering and Technology, Sun Yat-sen University, Zhuhai 519082, China
[b] Schulich Faculty of Chemistry, Technion-Israel Institute of Technology, Technion City, Haifa 32000, Israel
[c] Shenzhen Institute of Advanced Technology, Chinese Academy of Sciences, Shenzhen 518055, Guangdong, China

ABSTRACT

Replacing the sluggish O$_2$-producing half-reaction with value-added organic oxidations in water photolysis systems is deemed more practical to generate H$_2$ fuels. While loading of dual cocatalysts for both half-reactions onto nanoscale photocatalysts is highly beneficial for photocatalysis, developing such nanomaterials that are low-cost, stable and easy-to-synthesize remains challenging. Here, noble-metal-free CdS-Co$_3$O$_4$-NiS$_x$ nanodumbbells with spatially separated half-reaction sites are designed to simultaneously generate H$_2$ and oxidize benzylamine without any sacrificial agent. In this nanoarchitecture, electron-collecting NiS$_x$ and hole-collecting Co$_3$O$_4$ are anchored at the tips and sidewall of CdS nanowires, respectively, to lower the proton reduction and benzylamine oxidation energy barriers, respectively, thus establishing a dual-functional photocatalytic redox system. With significantly promoted charge separation and half-reaction kinetics, the nanodumbbells can produce H$_2$ (47 mmol$\bullet$g$^{-1}\bullet$h^{-1}) ca. 70 times faster than pure CdS, along with simultaneous benzylamine oxidation. Our findings provide a viable one-dimensional photocatalyst design strategy for various coupled half-reactions.

1. Introduction

Solar-driven hydrogen fuel production via photocatalytic overall water splitting (OWS) is deemed as a promising, cost-effective and environmentally benign technology, which aims to address the rapidly increasing global energy demand and ever-deteriorating environmental issues [1,2]. However, the energy conversion efficiency of OWS (2 H$_2$O → 2 H$_2$ + O$_2$) is largely restricted by the sluggish kinetics of the oxygen evolution reaction (OER) that involves the transfer of four electrons (2 H$_2$O→4 H$^+$+4e$^-$+O$_2$) [3–5]. Moreover, the O$_2$ by-product with low commercial value may lead to a serious back-reaction with H$_2$ and safety hazards, which requires costly gas separation [6]. To boost photocatalytic H$_2$ production, a commonly employed strategy is to add sacrificial hole scavengers, which not only completely wastes the oxidizing capability of the excited holes, but also is impractical in real-world scenarios due to the increased complexity and costs [7]. Recently, to couple hydrogen evolution reaction (HER) with value-added organic transformation reactions in photocatalytic systems has been proposed, which represents a more ideal technology compared

to OWS [8,9]. For instance, benzylamine oxidation reaction (BOR) with lower electrochemical potential (+0.76 V vs NHE) than OER (+1.23 vs NHE) [10], has been frequently introduced to photocatalytic HER systems because it allows the production of easily-separable N-benzylidenebenzylamine (N-BD), which contains an unsaturated C=N group and is a crucial intermediate for manufacturing pharmaceuticals, fine chemicals, and agrochemicals [4, 11–15]. However, developing photocatalysts with sufficient solar energy conversion efficiencies for coupled HER and BOR towards large-scale commercialization, especially low-cost catalysts with the absence of noble metal elements, remains challenging at the current stage [16].

One-dimensional nanostructures of cadmium sulfide (CdS), for instance, nanowires or nanorods, have been demonstrated highly efficient for photocatalytic HER in the presence of hole scavengers [17–19]. However, the CdS-based nanomaterials suffer severe photo-corrosion, due to the oxidation of S^{2-} by the photoexcited holes [20,21]. Auspiciously, the incorporation of BOR in CdS-based photocatalytic HER systems has been proven to be effective for the suppression of photo-corrosion [22]. Nevertheless, little has been done to investigate

---

* Corresponding author.
  E-mail address: xingzh7@mail.sysu.edu.cn (Z. Xing).

the spatial separation of HER and BOR active sites via loading dual co-catalysts onto CdS-based photocatalysts, although photocatalysts loaded with dual cocatalysts, which possess low over-potentials for half reactions, at different locations are found to not only allow the charge flow in selective directions, but also provides abundant active sites for both half reactions [23]. Lately, Yong and colleagues selectively deposited Pt and IrO$_x$ cocatalysts at different locations of g-C$_3$N$_4$/TiO$_2$ hollow nanospheres and realized efficient solar water splitting [24]. Noteworthily, site-selective deposition of dual cocatalysts on photocatalysts often involves complex synthetic procedures and utilization of noble metals (or metal oxides) in the past, which inevitably increases the fabrication cost and restricts the application [25–27]. Therefore, it will be extremely valuable if one can construct one-dimensional CdS nanostructures with spatially separated dual noble-metal-free cocatalysts for coupled photocatalytic HER and BOR. In recent years, transition-metal-based sulfides and oxides have been extensively investigated as potential low-cost alternatives for noble-metal-based cocatalysts for various reactions [28]. Among them, amorphous NiS$_x$ with enriched electron trapping/reduction active sites and weakened bonds to the adsorbed H species (S-H$_{ads}$) is reported to be a promising HER cocatalyst [29], and Co$_3$O$_4$ is found to be highly advantageous for BOR [30], which naturally encourages us to construct one-dimensional CdS nanoarchitecture with spatially separated NiS$_x$ and Co$_3$O$_4$ to significantly boost the efficiency of coupled photocatalytic HER and BOR.

Herein, we report the facile fabrication of a one-dimensional noble-metal-free CdS-Co$_3$O$_4$-NiS$_x$ photocatalyst (CdS-Co-Ni) with a nano-dumbbell architecture, in which NiS$_x$ is anchored at both ends of CdS nanowires (NWs) as the electron collector and HER cocatalyst, while Co$_3$O$_4$ is deposited on the sidewall of NWs as the hole collector and BOR cocatalyst. The photoexcited electrons and holes within the CdS NWs flow to the NiS$_x$ tips and the Co$_3$O$_4$ nanoislands on the sidewall, respectively, where subsequent H$_2$ generation from proton reduction and oxidation of benzylamine (BnNH$_2$) to valuable N-BD occurs simultaneously in the absence of any sacrificial agent. Remarkably, the rationally designed CdS-Co-Ni photocatalyst exhibited an outstanding H$_2$ generation rate of 47 mmol•g^{-1}•h^{-1}, with a maximal apparent quantum efficiency (AQE) of 45 % at 405 nm, ca. 70 times higher than that of pure CdS NWs, along with noticeable simultaneous BnNH$_2$ oxidation, surpassing most of the other reported systems of coupled photocatalytic HER and BOR by half an order of magnitude (Table S1).

2. Experimental section

2.1. Synthesis of Co$_3$O$_4$-decorated CdS nanowires

CdS nanowires were prepared via the typical solvothermal method according to our previous report [31]. CdS-Co$_3$O$_4$ nanostructures (CdS-Co) were prepared in a modified procedure according to the literature [32]. Briefly, a certain amount of Co(II) acetate tetrahydrate was added into 2.5 mL benzyl alcohol and stirred for 2 h. Later, 2.5 mL ammonium hydroxide (25 %) solution was dropwise added into the above mixture and then 50 mg of CdS powder was dissolved in the mixture by sonication. The solution was put into an oil bath and kept at 165 °C for 2 h under continuous stirring. Afterwards, diethyl ether was added to the reaction solution and the resulting product was washed with ethanol. The CdS-Co nanowires with different amounts of Co$_3$O$_4$ can be synthesized with the same synthesis procedure by using 5, 12.5, 25, 37.5, and 50 mg of Co(II) acetate tetrahydrate as the precursor, respectively, which are corresponding to CdS-Co(0.1), CdS-Co(0.25), CdS-Co(0.5), CdS-Co(0.75), and CdS-Co(1) based on the mass ratio of Co(II) acetate and CdS, respectively. Similarly, pure Co$_3$O$_4$ was prepared by the same procedure without CdS addition.

2.2. Synthesis of CdS-Co$_3$O$_4$-NiS$_x$ nanodumbbells

The subsequent oriented self-assembly of NiS$_x$ onto the tips of CdS-Co nanowires was achieved by a selective adsorption in-situ photo-deposition way. In a typical procedure, 1.5 mL Ni(NO$_3$)$_2$•6 H$_2$O and 1.5 mL thioacetamide aqueous solution were mixed to form Ni(II)-thioacetamide (Ni-TAA) complex (concentration ratio, r(thio-acetamide: Ni^{2+}) = 10). After that, 3 mg of the above CdS-Co was dissolved in 3 mL H$_2$O and then mixed with 1.5 mL ethanol, and 3 mL Ni-TAA aqueous solution. After purging with argon for 30 min, the above suspension was illumined by two LED illuminants (455 nm and Neutral white (MNWHL4, 375 nm~775 nm), 150 mW) for a certain time. Finally, the products were then collected and washed with DI water and ethanol. To study the amount of NiS$_x$ on the photoactivity of CdS-Co nanowires, the precursor concentration of Ni(NO$_3$)$_2$•6 H$_2$O was controlled to be 0.01, 0.025, 0.05, 0.075, 0.1 mol/L, respectively, and the achieved samples were represented as CdS-Co(n)-Ni(0.1), CdS-Co (n)-Ni(0.25), CdS-Co(n)-Ni(0.5), CdS-Co(n)-Ni(0.75), and CdS-Co(n)-Ni (1), respectively, where the n denotes above Co$_3$O$_4$ content. The NiS$_x$ modified CdS nanowires (CdS-Ni) were fabricated through an identical photodeposition route as the CdS-Co(n)-Ni(0.5) by replacing CdS-Co with CdS nanowires.

2.3. Synthesis of asymmetrical CoS$_x$ and MoS$_x$ tipped CdS-Co or CdS nanowires

In this case, the asymmetrical CoS$_x$ and MoS$_x$ tipped CdS-Co or CdS nanowires were synthesized under an identical procedure as the CdS-Co (0.25)-Ni(0.5) and CdS-Ni(0.5), while the Ni(NO$_3$)$_2$•6 H$_2$O was replaced by Co(NO$_3$)$_2$ or sodium molybdate.

2.4. Materials characterization

The crystal phase properties of samples were analyzed with an X-ray powder diffraction (XRD, Rigaku SmartLab 9 kW high-resolution diffraction system). Transmission Electron Microscopy (TEM) and Electron Dispersive Spectroscopy (EDS) were gained by an FEI Tecnai G^2 T20 S-Twin TEM (200 keV with a LaB6 electron source) and an FEI Titan 80–300KeV S/TEM with High Angle Annular Dark Field Scanning Transmission Electron Microscopy (HAADF-STEM) mode. Scanning electron microscopy (SEM) images were taken on a Zeiss Ultra-Plus HRSEM. UV-Vis absorption spectroscopy was taken using an Agilent Cary 5000 UV-Vis-NIR spectrophotometer. Photoluminescence (PL) measurements were carried out by using a Flourolog-3 Fluorometer at room temperature, using standard 10 mm fluorometer cuvettes. X-Ray Photoelectron Spectroscopy (XPS) spectra were gained in an analysis chamber using a Versaprobe III - PHI Instrument (PHI, USA). All binding energies were normalized based on the binding energy for the adventitious C1s line at 284.8 eV. ^{1}H NMR spectra were analyzed by a 300 MHz Bruker Advance spectrometer with CDCl$_3$ as the deuterated solvent. In-situ Kelvin probe force microscopy (KPFM) measurements were performed on a Bruker dimension fastscan equipped with a MESP probe model. Indium tin oxide (ITO, resistivity, 10 Ω·cm^{-2}) glass substrates, which were cleaned with acetone, ethanol and deionized water, were used to load samples. The CdS and CdS-Ni-Co$_3$O$_4$ nanowires were dispersed in ethanol solution and drop-casted onto the ITO substrates, followed by drying under ambient conditions. Patterns were acquired at scan rates of 0.5 Hz and the tip (Co/Cr coated Si tip, resonance frequency: 66 kHz) lift height was set to 100 nm at tapping mode for potential mapping. The compensate voltage was applied to the tip and the image of the Kelvin probe signal represented the relative scale of the electrostatic potential on the sample surface. The surface potential of each sample was measured under the same conditions in dark and light. The light source was from a fiber optic illuminator system with a 150 W halogen lamp.

2.5. Photocatalytic hydrogen production tests

The H$_2$-generation/benzylamine oxidation activities were evaluated in a custom-built gas-tight reaction cell connected to a 10 mL/min argon line (filtered 99.9999 % purity). In a typical measurement, 2 mg of the prepared catalyst was dispersed into 10 mL water-acetonitrile (60/40) mixtures containing 546 μl benzylamine (BnNH$_2$). After purging with argon (0.5 h), the samples were illuminated with a 405 nm LED adjusted to 50 mW (equivalent to a photon flux of 1.02×10^{17} photons/sec). The evolved hydrogen gas was analyzed by an online gas chromatograph (Agilent 7890 A with a 5 Å molecular sieve column and a thermal conductivity detector). For the cycling tests, the above system with fresh BnNH$_2$/acetonitrile aqueous solution was re-bubbled with argon to evacuate the H$_2$ products and the catalysts were recycled for the next H$_2$-generation measurement. The evolving H$_2$ was recorded in continuous flow mode which allows for direct evaluation of the gas production rate. The apparent quantum efficiencies (AQE) of H$_2$ evolution were calculated based on the following equation: $AQE = 2N_{H_2}/N_{h\nu}$, where N_{H_2} and $N_{h\nu}$ are the number of generated hydrogen molecules and the number of incident photons, respectively. The oxidation products were analyzed by means of gas chromatography-mass spectrometry (GC-MS) with dodecane as an internal standard.

2.6. Photoelectrochemical measurements

The photoelectrochemical properties were studied via employing a three-electrode electrochemical apparatus (SP-300, Bio-Logic SAS, France) in a 0.5 M Na$_2$SO$_4$ electrolyte including 0.1 M BnNH$_2$ with Fluorine doped Tin Oxide (FTO) glass (loading with catalysts), Ag/AgCl, and platinum foil as working, reference, and counter electrodes, respectively. The working electrode was fabricated via dropping 30 μl sample mixed slurry containing 2.5 mg of as-prepared products and a solution of DI water (350 μl) and 20 μl of Nafion onto the FTO substrate and dried for 8 h at 90 °C under N$_2$ gas condition with a mass loading of about 0.2 mg•cm^{-2}. The transient photocurrent (*i-t*) was measured with the LED irradiator (405 nm, 50 mW) on and off at a fixed interval of 1 min

All potentials were converted to a reversible hydrogen electrode (RHE) by employing the following equation: $E_{RHE} = E_{Ag/AgCl} + 0.1976 + 0.059$ pH. Linear sweep voltammetry (LSV) was recorded at a scan rate of 50 mV·s^{-1}. Tafel plots were obtained by replotting polarization curves as overpotential (η) vs. log current (logJ) based on the Tafel equation (η = b*log (J) + a). Electrochemical impedance spectroscopy (EIS) was measured in 100 kHz-0.01 Hz (frequency). Mott-Schottky (M-S) plots were carried out via using a frequency of 1.0 kHz and an amplitude of 5 mV.

3. Results and discussion

3.1. Synthesis of the CdS nanowires with spatially separated cocatalysts

The preparation of CdS-Co-Ni nanodumbbells followed a facile two-step route (Fig. 1), that is, chemical deposition of Co$_3$O$_4$ nanoparticles (NPs) onto the sidewalls of CdS NWs (CdS-Co NWs, step 1) and the subsequent photodeposition of NiS$_x$ at the tips of the CdS NWs (CdS-Co-Ni NWs, step 2). The CdS NWs (Fig. S1a) synthesized via a solvothermal method according to our previous report possessed an average diameter of ca. 50 nm and a length of several hundred nm, as confirmed by scanning electron microscopy (SEM) (Fig. S1b) and transmission electron microscopy (TEM) (Fig. S1c) [17,31]. The XRD results (Fig. 3a) indicated a hexagonal wurtzite CdS (JCPDS no. 77–2306) crystal structure. The as-prepared CdS NWs were first deposited with Co$_3$O$_4$
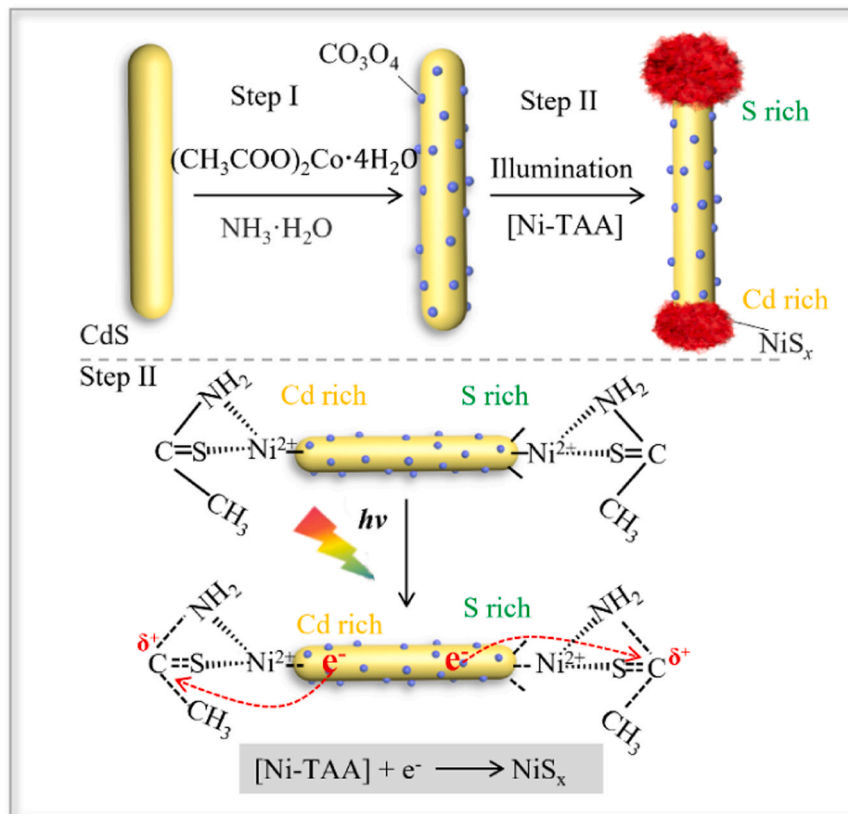
Fig. 1. Schematic illustration of the synthesis route of NiS$_x$ tipped CdS-Co NWs. The alternating atomic planes (S-Cd-S-Cd) in the [001] direction of the CdS NWs lead to asymmetric Cd-rich and S-rich terminations at the opposite ends of the NWs, which endow the two ends with different chemical affinities for the subsequent reaction.
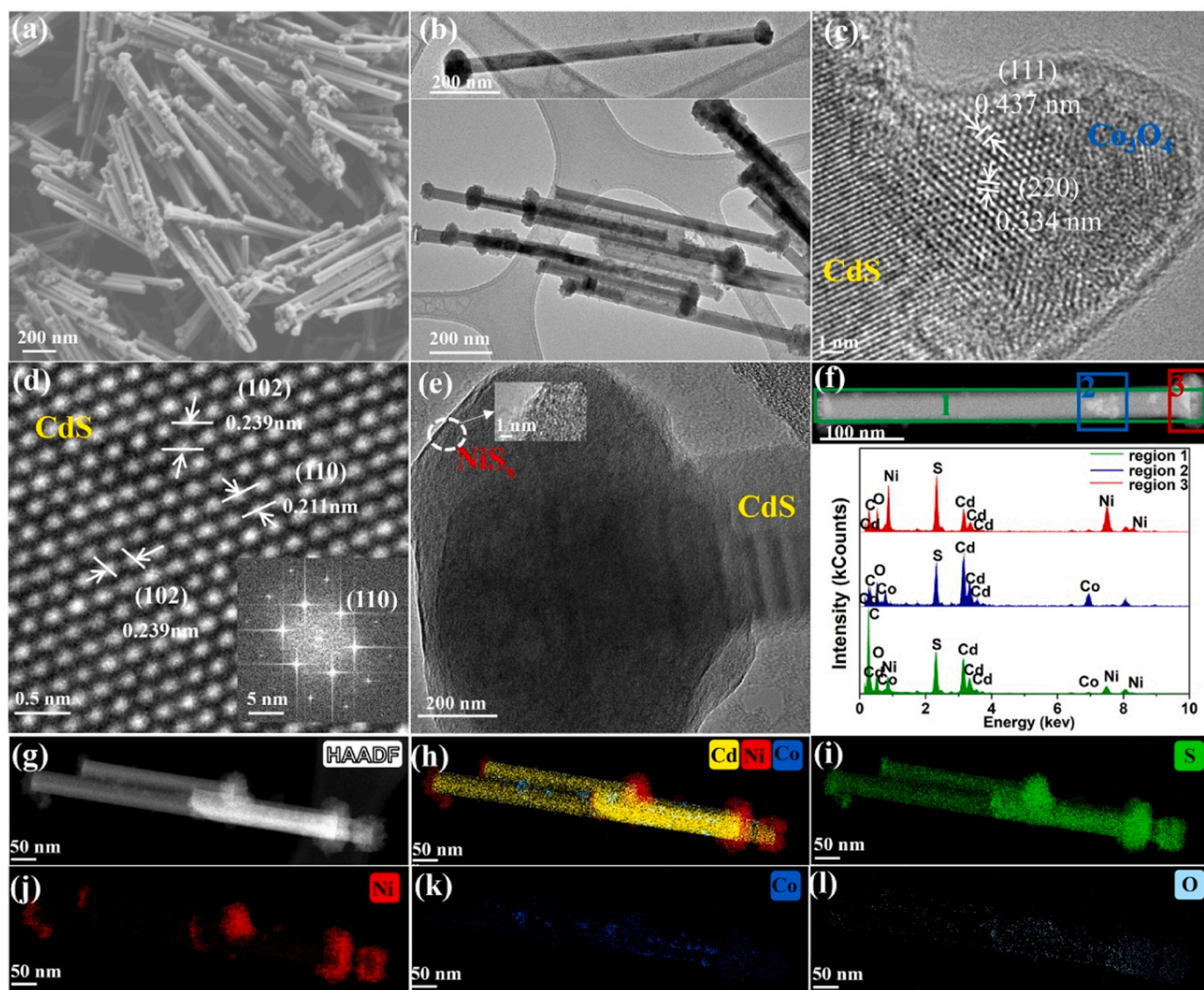
Fig. 2. (a) SEM and (b, c, e) TEM and HRTEM images of CdS-Co-Ni nanowire. (d) The corresponding atomic resolution HRTEM image for selected CdS part in CdS-Co-Ni nanowire. (f) STEM-EDS spectra recorded from different regions of single CdS-Co-Ni nanowire shown in the HAADF image. (g) HAADF-STEM image and (h-l) corresponding elemental maps of CdS-Co-Ni nanowires.

nanoislands via a versatile oil-bath-assisted reaction, the amount of which can be tuned by changing the concentration of cobalt(II) acetate precursor (the obtained samples are named as CdS-Co(n) NWs, n: mass ratio between cobalt(II) acetate and CdS). Larger n led to the growth of more Co_3O_4 NPs with an average size of 3–6 nm onto the CdS NWs and eventually the surface of CdS NWs became mostly covered with numerous Co_3O_4 nanoislands (Fig. S2). The successful deposition of Co_3O_4 was further verified by the SEM image (Fig. S3a), high-angle annular dark-field scanning TEM (HAADF-STEM) image (Fig. S3b) and the corresponding elemental maps (Fig. S3c-g) collected with energy-dispersive X-ray spectroscopy (EDX).

The Co_3O_4-decorated CdS NWs were then deposited with NiS_x clusters via photodeposition in the presence of a Ni(II)-thioacetamide (Ni-TAA) complex, a single source precursor similar to MoS_4^{2-} and diethyldithiocarbamate metal complexes [33–38]. Successful decoration of NiS_x on CdS-Co NWs was verified by SEM and TEM images of CdS-Co-Ni NWs (Fig. 2a&b), where the cap-shaped NiS_x was symmetrically tipped on both edges. The XRD results (Fig. 3a) not only indicated the wurtzite CdS crystal structure being preserved in the CdS-Co-Ni NWs with the non-shifted peaks, but also verified the introduction of cubic phase

Co_3O_4 (JCPDS no. 42–1467) and amorphous nature of the NiS_x tips. High-resolution TEM (HRTEM) (Fig. 2d) and the corresponding fast Fourier transform (FFT) pattern (inset of Fig. 2d) of CdS-Co-Ni NWs showed the lattice spacings of 0.239 and 0.211 nm assigned to the (102) and (110) planes of CdS, respectively. The HRTEM image captured near the CdS-Co_3O_4 boundary of CdS-Co-Ni NWs (Fig. 2c) showed that the crystal lattices of CdS smoothly transition to the Co_3O_4 NPs with a subtle lattice distortion. The observed interplanar spacings of 0.437 and 0.334 nm of the Co_3O_4 NPs are ascribed to (111) and (220) planes, respectively (Fig. 2c). The amorphous NiS_x decorated at the ends of CdS-Co NWs was confirmed by an enlarged view of the HRTEM image (Fig. 1e) and the HAADF-STEM image (Fig. S4). The spatially separated distribution of Co_3O_4 and NiS_x can be clearly visualized by the STEM-EDS spectra recorded at different positions of a single CdS-Co-Ni NW (Fig. 2f) and elemental mapping (Fig. 2g-l). While a complete CdS-Co-Ni NW contained Cd, Ni, Co, S, and O (Fig. 2f, region 1), the sidewall exhibited elements belonging to CdS and Co_3O_4 (region 2) and the end (region 3) presented the main signals of Cd, Ni and S. Elemental maps (Fig. 2g-l) further confirmed that S is homogeneously distributed throughout the dumbbell shaped NWs, Ni concentrates at the tips and
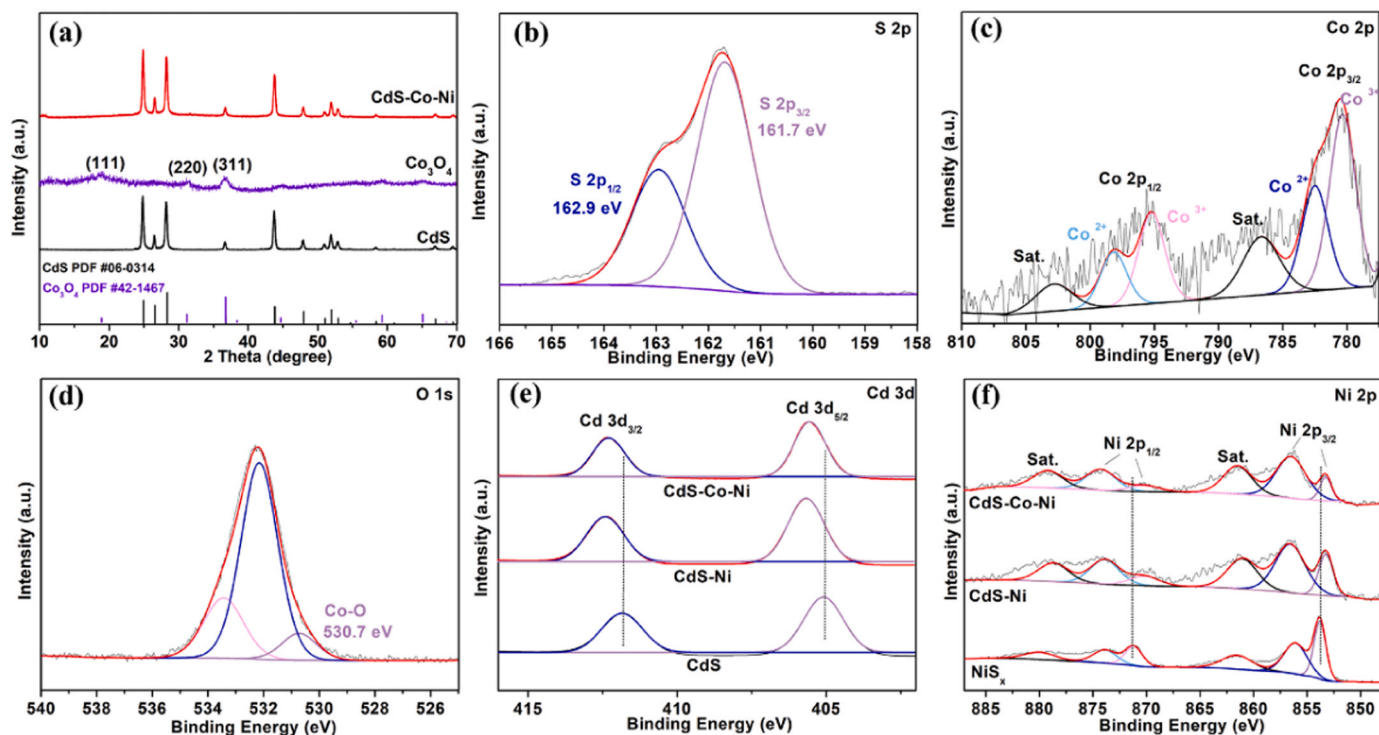
Fig. 3. (a) Schematic illustration of XRD patterns of as-prepared samples. High-resolution XPS spectra of S 2p (b), Co 2p (c) and O 1 s (d). High-resolution Cd 3d (e) and Ni 2p (f) XPS spectra of CdS, CdS-Ni and CdS-Co-Ni.

Cd, Co and O are limited to the stem part. Therefore, in a CdS-Co-Ni NW, the NiS_x was confirmed to locate at both ends of the CdS NW, with the Co_3O_4 NPs deposited on the sidewall, featuring a nanodumbbell structure.

In order to reveal the mechanism for the selective growth of NiS_x onto the ends of the CdS-Co NWs, we attempted to study the growth process via tuning synthesis parameters including precursor concentration and type, illumination time, etc. Higher concentrations of the Ni-TAA precursor led to symmetric NiS_x tips of bigger sizes at both ends of the CdS-Co NWs (Fig. S5a-d), but at the highest concentration, the tips seemed to be unstable and shattered to small particles (Fig. S5e). Furthermore, variation of the illumination time caused little difference to the NiS_x tipping (Fig. S6), and the photochemical reaction can be completed within 5 min (also reflected by the fast color changing to dark). Our earlier works showed that the CdS NWs stretch along the [001] axis, which endows alternating lattice planes of S and Cd atoms (S-Cd-S-Cd) in the [001] direction of the CdS crystal structure [17,31]. The Cd-terminated and S-terminated ends of the 1D CdS NWs possess different affinities for the Ni-TAA precursor due to different charge attractions [39], leading to a bigger NiS_x cluster at the S-terminated end. Generally, the greater surface energy at the tips of 1D CdS NWs than that along the body favors the preferential growth of metal particles at the tips, and the tips may also act as isolated nucleation sites due to the much larger lengths of CdS NWs relative to the size of the metal particles [39,40]. In addition, 1D semiconductors provide a unique charge migration path along the longitudinal axis, guiding the electrons to the tips under illumination [41,42]. Therefore, during the photodeposition process, the energetics at the CdS apex facets and unique charge transportation along the longitudinal axis may be the main reasons for the preferential photoreduction of Ni-TAA at the tips of NWs. It is worth noting that thiourea, which possesses a similar molecular structure to TAA, can also form a complex with Ni and be used to selectively deposit NiS_x at the tips of NWs (Fig. S7), while Na_2S caused fast precipitation of Ni ions and was unable to initiate any tipping, highlighting the importance of Ni complex precursor to the NiS_x tipping. In addition, the NiS_x

tipping on the bare CdS NWs can also be achieved under identical conditions, as shown in Fig. S8.

To demonstrate the universality of selective cocatalyst photodeposition onto 1D CdS nanostructures, tipping with Co and Mo sulfides were examined via similar protocols. Interestingly, while symmetric CoS_x tips were observed at both ends of the CdS (or CdS-Co) NWs, only one end of NWs was tipped with MoS_2 (Fig. S9). Although the growth of metal tips on 1D semiconductors has been reported in the past [43–46], the tipping behaviors and underlying mechanisms for symmetrical and asymmetrical tips remain unclear. Park et al. believed that the difference in the affinity of various Mo precursors to the two ends of CdS NWs results in either single or double MoS_2 tips [47]. It is speculated that the different affinity towards the metal precursors of the Cd-terminated and S-terminated ends of the CdS NWs led to different tipping behaviors.

3.2. Chemical structures of the CdS-Co-Ni NWs

The chemical structures of the obtained nanomaterials were investigated with X-ray photoelectron spectroscopy (XPS). The XPS survey spectrum of CdS-Co-Ni NWs (Figure. S10a) proved the coexistence of Cd, Co, Ni, S and O elements, further reflecting the successful introduction of Co_3O_4 and NiS_x onto the CdS NWs. In the high-resolution S 2p spectrum of CdS-Co-Ni NWs (Fig. 3b), two separate peaks at 162.9 and 161.7 eV are indexed to S $2p_{1/2}$ and S $2p_{3/2}$ of S^{2-}, respectively. Moreover, a slight shift of S 2p peaks (Fig. S10b) towards the lower binding energy region was observed after Co_3O_4 loading compared to pure CdS, indicating the accumulation of more free electrons at CdS due to a strong electron coupling effect between CdS and Co_3O_4. The fitted Co 2p XPS spectrum of CdS-Co-Ni hinted the coexistence of Co^{3+} and Co^{2+}, as expected for Co_3O_4 (Fig. 3c). In the O 1s spectrum of CdS-Co-Ni (Fig. 3d), the peak at 530.7 eV corresponds to Co-O and the other two peaks at 532.2 and 533.4 eV are related to the surface oxygenated groups (O-H, C-O). The doublet peaks at 405.0 and 411.8 eV of the high-resolution Cd 3d spectrum of pure CdS NWs slightly shifted towards higher binding energy regions upon the introduction of NiS_x (Fig. 3e), reflecting the

intimate interfacial interaction that reduces the electron density at CdS. The Ni 2p peaks of both CdS-Ni and CdS-Co-Ni displayed negative shift in binding energy compared to pure NiS_x, further unraveling the electron transfer from CdS to NiS_x (Fig. 3f). Therefore, strong electric coupling at both the CdS/Co_3O_4 and CdS/NiS_x interfaces has been revealed in the CdS-Co-Ni, which has been proved to lay solid foundations for charge flow across material interfaces [48–51].

3.3. Coupled photochemical HER and BOR

The UV–vis diffuse reflectance spectroscopy (DRS) showed that the optical absorption edge of the pure CdS NWs was positioned at 508 nm (Fig. 4a), and the black Co_3O_4 and NiS_x powder presented strong optical absorption in the broad range of 300–800 nm. The introduction of dual cocatalysts onto the CdS NWs had little effect on the absorption edge but enhanced the background absorption beyond the absorption edge. According to the Tauc plot, the band gap of pure CdS can be calculated to be 2.44 eV (Fig. 4b) [52]. Additionally, the Mott-Schottky (M-S) curve of CdS exhibited a positive slope, typical for n-type semiconductors (Fig. 4c), and its flat band potential was found to be − 0.61 V versus NHE, which is conventionally considered near the conduction band (CB) edge of n-type CdS. Thus, the valence band (VB) edge of CdS was calculated to be 1.83 V versus NHE. The above results prove that coupled HER and BOR are thermodynamically feasible for the CdS NWs used in this work.

Given the favorable energetics of the CdS NWs for both HER and BOR, coupled photocatalytic HER and BOR were examined with the as-prepared samples under visible light illumination (405 nm) without any sacrificial agents. The cocatalysts, that is, Co_3O_4 and NiS_x alone generated negligible H_2 with maximum apparent quantum efficiencies (AQEs)

of 0.3 % and 1.4 %, respectively (Fig. S11). Moreover, although the bare CdS NWs exhibited a rather low HER rate of 0.66 mmol•g^{-1}•h^{-1} (Fig. 5a) with a maximum AQE of 0.5%, possibly due to the fast charge recombination and insufficient active sites [53], the loading of Co_3O_4 nanoislands and NiS_x tips drastically improved the photocatalytic activities (Fig. S12). The CdS NWs deposited with Co_3O_4 NPs at the optimal content (CdS-Co(0.25)) can produce H_2 at a rate of up to 10 mmol•g^{-1}• h^{-1} (Fig. 5a) with an AQE of 8.2% (Fig. S12a, Fig. 5a&b). Even more impressively, to further decorate the CdS-Co(0.25) with NiS_x tips elevated the AQE to another level (Fig. S12b), with the best performer, CdS-Co(0.25)-Ni(0.5), demonstrating a photocatalytic HER rate of, astonishingly, 47 mmol•g^{-1}•h^{-1}, ca. 70 times higher than that of pure CdS NWs (Fig. 5a), and a total amount of 229 mmol•g^{-1} of H_2 was accumulated after 5 h of reaction (Fig. 5c). Loading the CdS NWs with the optimal ratio of NiS_x (CdS-Ni(0.5)) led to a higher photocatalytic HER rate (15 mmol•g^{-1}•h^{-1}), but still lower than that of CdS-Co (0.25)-Ni(0.5), highlighting the advantages of spatially separated dual cocatalysts. However, the addition of excessive Ni precursor during the synthesis process (CdS-Co(0.25)-Ni(1)) caused severe photochemical activity deterioration, which may be due to the noticeable morphological change as discussed earlier [47]. Although the AQE of CdS-Co (0.25)-Ni(0.5) gradually decreased with time as a result of reduced concentration of $BnNH_2$ (Fig. 5d), the HER activity was quickly restored upon the injection of fresh $BnNH_2$ and the AQE was still higher than the non-tipped CdS NWs even after 20 h of illumination (Fig. S12c). Under irradiation by a solar simulator equipped with a standard AM 1.5 G filter and output power density of 24 mW•cm^{-2}, CdS-Co(0.25)-Ni(0.5) can produce H_2 at a rate of 0.015 mmol•h^{-1} with a maximum solar-to-chemical (STC) efficiency of 1.3 % (Fig. S13).

Noteworthy is the fact that the CdS NWs tipped with other transition
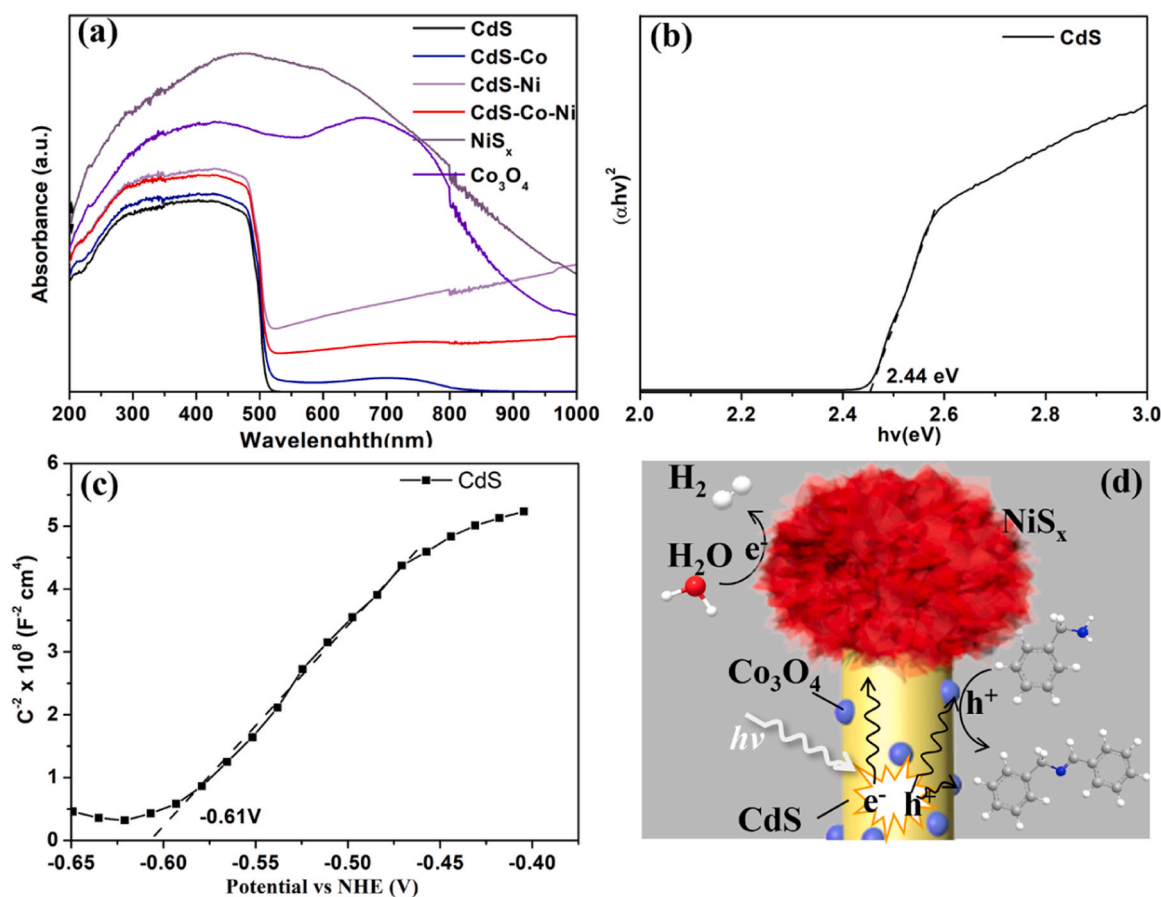
Fig. 4. (a) UV–vis DRS of CdS, CdS-Co, CdS-Ni and CdS-Co-Ni NWs. (b) Tauc plots and (c) Mott-Schottky plots of pure CdS. (d) schematic representation of the proposed photochemical redox reaction mechanism of CdS-Co-Ni NWs.
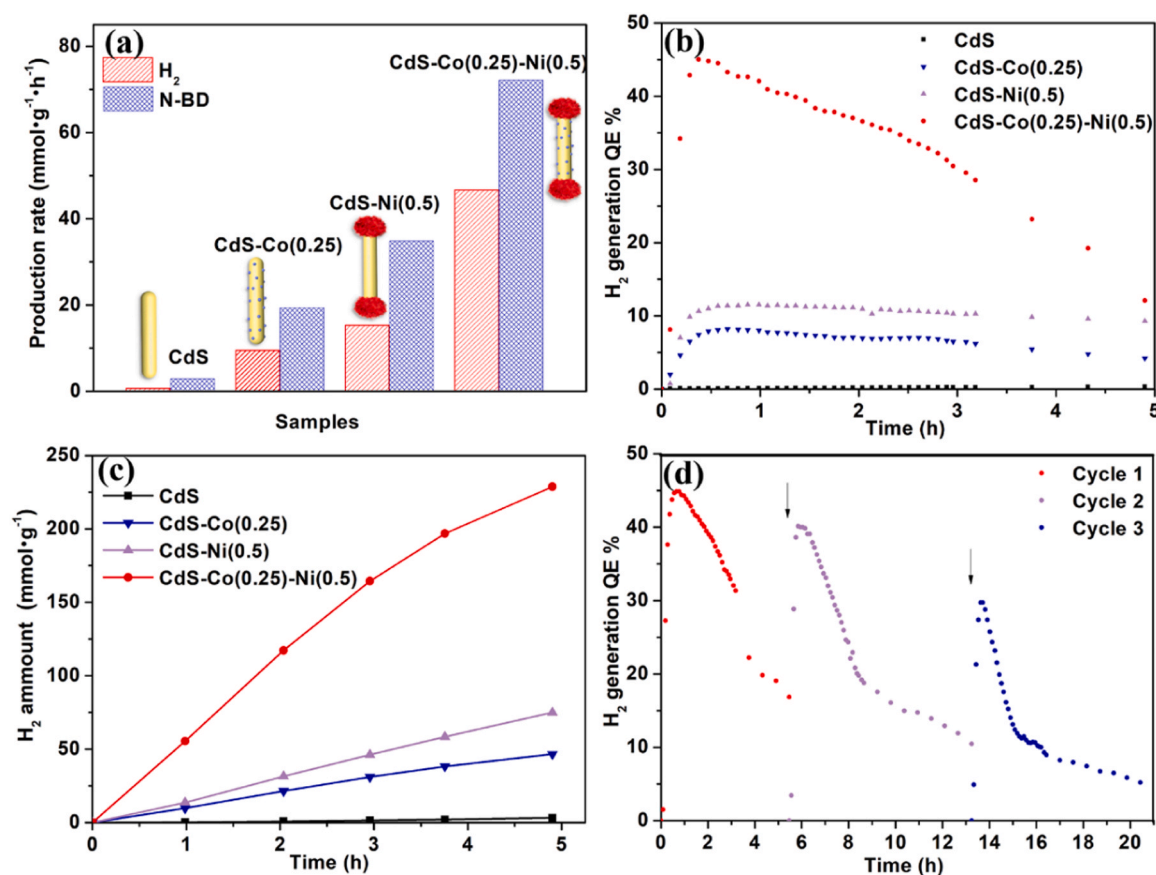
Fig. 5. (a) Average photocatalytic H_2 evolution rates, (b) real-time apparent quantum efficiency and (c) H_2 generation time profiles of pure CdS, CdS-Co(0.25), CdS-Ni(0.5) and CdS-Co(0.25)-Ni(0.5). (d) Cycling runs of CdS-Co(0.25)-Ni(0.5) for photocatalytic H_2 evolution. The addition of fresh BnNH$_2$ in H_2O/CH_3CN (60/40) solvent during the irradiation is marked by black arrows.

metal sulfides as the HER cocatalyst also achieved enhanced photocatalytic activities compared to the non-tipped counterparts. The decoration CoS$_x$ and MoS$_x$ tips on the CdS NWs boosted the H_2 evolution rates to 7.8 and 2.3 mmol•g^{-1}•h^{-1}, respectively, which were further increased to 11.7 and 14.2 mmol•g^{-1}•h^{-1}, respectively, upon the deposition of Co$_3$O$_4$ nanoislands on the sidewall (Fig. S14a). However, the CoS$_x$ and MoS$_x$ tipped CdS-Co NWs exhibited dramatically lower maximum AQEs for HER (12 % and 15 %, respectively) and total amount of accumulated H_2 (144 and 175 mmol•g^{-1}, respectively, after 12.35 h) as compared to the NiS$_x$ tipped counterpart (45 %, 330 mmol•g^{-1}), indicating that NiS$_x$ is a superior reduction cocatalyst for this system (Fig. S14b&S14c).

To verify the coupling between the HER and BOR half reactions in our photocatalytic system, a control experiment without BnNH$_2$ was conducted for CdS-Co(0.25)-Ni(0.5), in which only a minimal amount of H_2 can be generated (maximum AQE of 0.25 %, Fig. S15a), clearly demonstrated the importance of BOR to the overall photocatalytic reaction. More importantly, the protons released from the oxidation process of BnNH$_2$ ($\underline{2BnNH_2 + 2h^+ \rightarrow N\text{-}BD + NH_4^+ + H^+}$) [54,55] were found to partially contribute to the HER process. In a control experiment, photocatalytic coupled HER and BOR was carried out in pure acetonitrile (99.7 %) solvent, and CdS-Co(0.25)-Ni(0.5) only exhibited a maximum AQE of 24 % for H_2 generation (Fig. S15b), which is noticeably lower than that in the H_2O/acetonitrile mixture (45 %), suggesting that the H_2 produced in the photocatalytic reaction was originated from both water and protons released from benzylamine oxidation. The products of photocatalytic BnNH$_2$ oxidation were analyzed via gas chromatography mass spectrometry (GC-MS). N-benzylidenebenzylamine (N-BD) with a molecular weight of 195 and a fragmentation pattern with a molecular ion peak at $m/z = 91$, corresponding to PhCH$_2$,

was identified as the main product of BOR from the MS spectrum (Fig. S16b) [11]. In addition, two peaks at chemical shifts of 4.82 and 8.39 ppm assigned to the imine protons of N-BD were detected in the ^{1}H NMR spectra (Fig. S16c) of the extracted mixture after 5 h of photocatalytic reaction, further verifying that the generated N-BD was a product of BOR [11]. With prolonged illumination, a higher percentage of BnNH$_2$ was converted to N-BD over CdS-Co-Ni, with growing peaks assigned to N-BD and lowering signals of BnNH$_2$ in the GC spectra (Fig. S16a). Aside from the astounding HER activity, the CdS-Co(0.25)-Ni(0.5) also exhibited highly efficient N-BD production at a rate of ca .72 mmol•g^{-1}•h^{-1}, which is noticeably superior than the bare CdS NWs (2.7 mmol•g^{-1}•h^{-1}) and those loaded with single cocatalyst (19.1 and 34.6 mmol•g^{-1}•h^{-1} for CdS-Co and CdS-Ni, respectively) (Fig. 5a), highlighting the advantage of the CdS-Co-Ni nanodumbbell architecture for the coupled photocatalytic HER and BOR.

3.4. Charge separation induced by the loading dual cocatalysts

Despite the intactness of the CdS NWs after dual cocatalysts loading and the low intrinsic activities of single catalysts, impressive coupled photocatalytic HER and BOR were observed with the CdS-Co-Ni nanodumbbells, which is naturally believed to be owing to the significantly improved charge separation and surface reaction kinetics, as we expected. The separation behavior of the photoinduced charges has been investigated with in-situ Kevin-probe force microscopy (KPFM) measurements, in which the contact potential difference (CPD) between the scanning tip and the surface of the specimen was monitored under different illumination conditions. As depicted in Fig. 6a-d, the average CPD measured across the diameter of the CdS NWs shifted negatively by 11.4 mV (from ca. 350–338.6 mV) upon illumination. The co-loading of
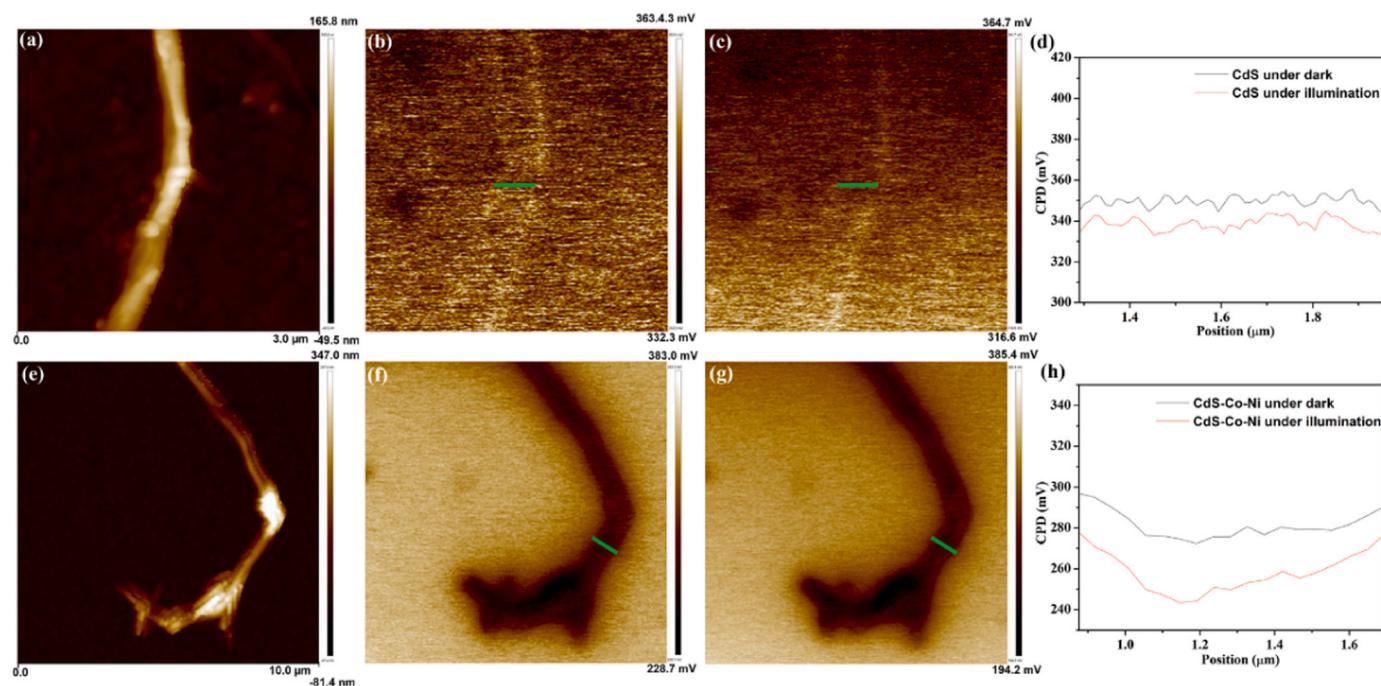
Fig. 6. AFM and KPFM images under different illumination conditions of (a-c) pure CdS and (e-g) CdS-Co-Ni NWs respectively. CPD distributions obtained from the sample areas (green line) of the KPFM images of (d) pure CdS and (h) CdS-Co-Ni NWs, respectively.

Co_3O_4 and NiS_x cocatalysts onto the CdS NWs at selective locations not only shifted the intrinsic CPD to a lower value (281 mV) in the dark, but more importantly, led to a much larger CPD drop of 22.2 mV upon illumination (Fig. 6e-h), indicating the improved charge separation. The steady-state photoluminescence (PL) spectra reflected (Fig. S17a) that the free exciton recombination in the pure CdS NWs was significantly suppressed after loading the Co_3O_4 nanoislands, and further quenched after the subsequent decoration of NiS_x, suggesting the efficient charge extraction from CdS by the dual cocatalysts in the CdS-Co-Ni NWs to forestall the radiative recombination. Meanwhile, transient PL studies were carried out to further investigate the charge separation behavior of as-prepared samples (Fig. S17b and Table S2). As compared to the average PL lifetime (τ_{avg}) of pure CdS (3.78 ns), all the cocatalyst-loaded CdS NWs exhibited shortened average PL lifetime values. In particular, the CdS NWs decorated with dual cocatalysts at selective locations exhibited the smallest τ_{avg} of 2.96 ns, indicating the enhanced charge separation efficiency after cocatalyst loading [56,57]. This is in good agreement with our material design since the photoexcited electron-hole pairs generated in the CdS NWs are supposed to be effectively separated, with the electrons transferred to the NiS_x tips and the holes to the Co_3O_4 nanoislands.

The interfacial charge separation was further analyzed via electrochemical techniques. Compared to the pure CdS, CdS-Co and CdS-Ni, the CdS-Co-Ni NWs exhibited largely reduced charge-transfer resistance at the semiconductor-electrolyte interface, as confirmed by the smallest semicircle radius in the electrochemical impedance spectroscopy (EIS) Nyquist plots (Fig. S17c). The open-circuit potentials (OCP) of all the as-prepared samples shifted negatively upon illumination (Fig. 7a), which is typical for n-type semiconductors due to the formation of a depletion layer at the semiconductor-electrolyte interface and reflects the interfacial charge separation [58–60]. The larger ΔOCP of the CdS-Co-Ni NWs compared to those of CdS, CdS-Co and CdS-Ni NWs revealed that the loading of dual cocatalysts can more effectively restrict the surface charge recombination. Additionally, the derivative of OCP with respect to time (-d(OCV)/dt) was extracted from the initial stage of irradiation (Fig. 7b) and the CdS-Co-Ni NWs showed the largest initial -d(OCV)/dt value, which demonstrates its optimum charge separation [61]. The

greatly facilitated charge separation in CdS-Co-Ni as evidenced by the KPFM, PL and electrochemical tests, also brought about a noticeable boost to the anodic photocurrents measured with the photoelectrodes fabricated via drop-casting. As shown in Fig. S17d, the CdS-Co-Ni NWs produced the highest photocurrent density (ca. 5 $\mu A\bullet cm^{-2}$ at 0.7 V vs Ag/AgCl) under illumination among all the as-prepared samples (ca. 1 $\mu A\bullet cm^{-2}$ for CdS, ca. 2.5 $\mu A\bullet cm^{-2}$ for CdS-Co, ca. 3 $\mu A\bullet cm^{-2}$ for CdS-Ni), implying the superior charge carrier migration and separation after the deposition of the dual cocatalysts.

3.5. Enhanced HER and BOR catalytic kinetics

The way how the dual cocatalysts on CdS NWs changed the surface thermodynamics and kinetics for both the HER and BOR half reactions has been explored in depth via electrochemical analysis. In the cathodic linear sweep voltammetry (LSV) plots (Fig. 7c), the onset potentials of the CdS-Ni (−389 mV vs reversible hydrogen electrode, (RHE)) and CdS-Co-Ni NWs (−362 mV vs RHE) shifted positively compared to CdS (−467 mV vs RHE), and the overpotentials of CdS-Ni (935 mV) and CdS-Co-Ni (884 mV) at the current density of 10 $mA\bullet cm^{-2}$ were significantly smaller than that of CdS (beyond the scan range). The dramatically enlarged cathodic currents at the same bias and lower overpotentials with the introduction of HER cocatalyst, that is, the NiS_x tips, testifies the much lower thermodynamic energy barrier for HER at the tips. In addition, the decoration of NiS_x led to reduced Tafel slope values as calculated from the Tafel plots (Fig. 7d), with 84 $mV\bullet dec^{-1}$ for CdS-Ni and 49 $mV\bullet dec^{-1}$ for CdS-Co-Ni NWs as compared to 664 $mV\bullet dec^{-1}$ for CdS, suggesting the faster HER kinetics at the NiS_x cocatalyst. Similarly, in the anodic LSV plots measured in the presence of benzylamine (Fig. 7e), CdS-Co and CdS-Co-Ni possessed lower onset potentials (1.494 V vs RHE for both) than that of CdS (1.711 V vs RHE), and the corresponding Tafel slopes (Fig. 7f) of both CdS-Co and CdS-Co-Ni (560 and 329 $mV\bullet dec^{-1}$, respectively) were smaller compared to that of CdS (736 $mV\bullet dec^{-1}$). Therefore, the Co_3O_4 nanoislands on the CdS NWs can serve as active reaction sites for BOR, with reduced reaction overpotential and accelerated kinetics.

The greatly facilitated HER and BOR kinetics by the loading of dual
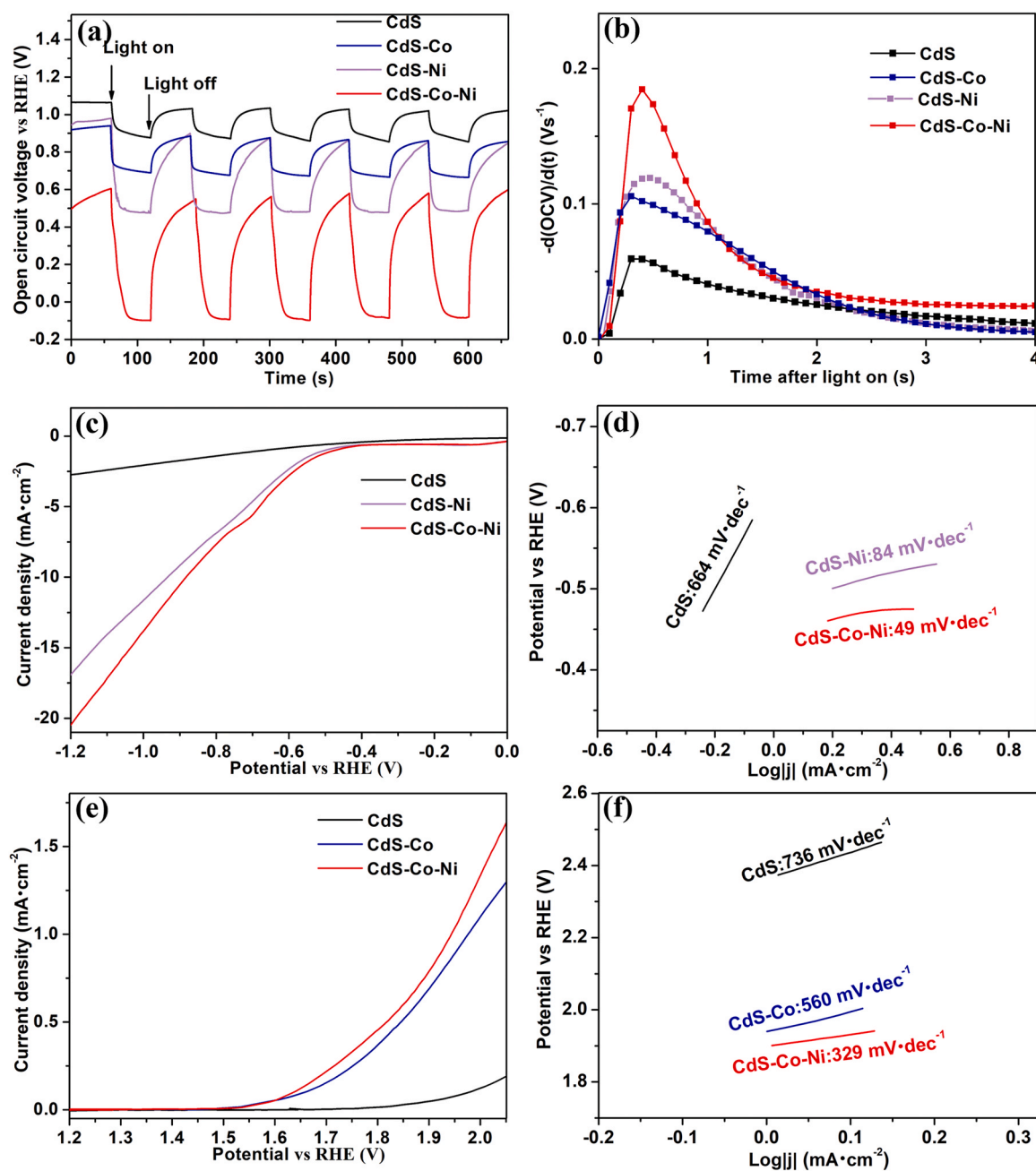
Fig. 7. (a) OCV response to light on/off and (b) Plots of the derivative of OCV with respect to time versus time upon light on of CdS, CdS-Co, CdS-Ni and CdS-Co-Ni NWs. (c) HER linear sweep voltammetry (LSV) curves measured under dark conditions and (d) Tafel plots of the samples. (e) Anode LSV curves measured under dark conditions and (f) corresponding Tafel plots. The photoelectrochemical tests were measured in 0.5 M Na_2SO_4 with 0.1 M benzylamine.

cocatalysts, combined with the smooth charge separation observed in the CdS-Co-Ni nanodumbbells, are thus believed to contribute to the excellent activities of coupled photocatalytic HER and BOR. In the rationally designed ternary catalyst, the spatially separated redox cocatalysts allow the photoinduced electrons of CdS to flow along the axial direction and be captured by the NiS_x reduction cocatalyst at both ends of CdS [62], where they combine with H^+ to generate H_2, while the holes are allowed to be trapped by the Co_3O_4 oxidization cocatalyst for organic transformation (Fig. 4d) [63].

4. Conclusions

In summary, we have developed a facile strategy to fabricate a one-dimensional nanoscale noble-metal-free ternary $CdS-Co_3O_4-NiS_x$ (CdS-

Co-Ni) photocatalyst, with Co_3O_4 nanoislands located on the sidewalls of the CdS NWs and NiS_x tips at both ends as the cocatalysts for both the proton reduction and benzylamine oxidation half reactions, respectively. The unique nanoarchitecture with well-defined spatially separated catalytic sites not only drives the photogenerated electrons and holes in the CdS stem to migrate directionally to the NiS_x tips and Co_3O_4 nanoislands, respectively, for efficient charge separation, but also provides favorable kinetics and markedly reduced energy barrier for HER and BOR, as evidenced by in-situ KPFM analysis as well as thorough electrochemical and spectral studies. As a result, under visible light irradiation in the absence of sacrificial agent, the optimized ternary NWs achieved an impressive H_2 generation rate of 47 mmol•g^{-1}•h^{-1}, ca. 70 times higher than that of pure CdS NWs, along with simultaneous benzylamine oxidation, which is comparable with previously reported

systems containing noble metals for coupled photocatalytic HER and BOR. The delicate nanoarchitecture design based on one-dimensional photocatalysts demonstrated in this work paves the way for constructing cost-effective photocatalysts with spatially separated reaction sites for high-efficiency coupled HER and possibly selective production of a gallery of value-added chemicals.

CrediT authorship contribution statement

Yuexing Chen: Conceptualization, Investigation, Methodology, Data curation, Writing – Original Draft. **Hui Xie**: Investigation, Methodology. **Ming Ma**: Software, Methodology. **Zheng Xing**: Supervision, Resource, Writing-review & editing, Funding acquisition.

Declaration of Competing Interest

The authors declare that they have no known competing financial interests or personal relationships that could have appeared to influence the work reported in this paper.

Data availability

Data will be made available on request.

Acknowledgments

Appendix A. Supporting information

Supplementary data associated with this article can be found in the online version at doi:10.1016/j.apcatb.2023.123433.

References

[1] Z. Wang, C. Li, K. Domen, Recent developments in heterogeneous photocatalysts for solar-driven overall water splitting, Chem. Soc. Rev. 48 (2019) 2109–2125.

[2] J. Gong, C. Li, M.R. Wasielewski, Advances in solar energy conversion, Chem. Soc. Rev. 48 (2019) 1862–1864.

[3] Y. Jiao, Y. Zheng, M. Jaroniec, S.Z. Qiao, Design of electrocatalysts for oxygen-and hydrogen-involving energy conversion reactions, Chem. Soc. Rev. 44 (2015) 2060–2086.

[4] H. Liu, C. Xu, D. Li, H.L. Jiang, Photocatalytic hydrogen production coupled with selective benzylamine oxidation over MOF composites, Angew. Chem. 130 (2018) 5477–5481.

[5] R.D. Smith, M.S. Prévot, R.D. Fagan, Z. Zhang, P.A. Sedach, M.K.J. Siu, S. Trudel, C. P. Berlinguette, Photochemical route for accessing amorphous metal oxide materials for water oxidation catalysis, Science 340 (2013) 60–63.

[6] S. Haussener, C. Xiang, J.M. Spurgeon, S. Ardo, N.S. Lewis, A.Z. Weber, Modeling, simulation, and design criteria for photoelectrochemical water-splitting systems, Energy Environ. Sci. 5 (2012) 9922–9935.

[7] X. Xiang, B. Zhu, J. Zhang, C. Jiang, T. Chen, H. Yu, J. Yu, L. Wang, Photocatalytic H_2-production and benzyl-alcohol-oxidation mechanism over CdS using Co^{2+} as hole cocatalyst, Appl. Catal. B Environ. 324 (2023), 122301.

[8] M.-Y. Qi, M. Conte, M. Anpo, Z.-R. Tang, Y.-J. Xu, Cooperative coupling of oxidative organic synthesis and hydrogen production over semiconductor-based photocatalysts, Chem. Rev. 121 (2021) 13051–13085.

[9] S. Kampouri, K.C. Stylianou, Dual-functional photocatalysis for simultaneous hydrogen production and oxidation of organic substances, ACS Catal. 9 (2019) 4247–4270.

[10] M. Zhang, Y. Mao, X. Bao, G. Zhai, D. Xiao, D. Liu, P. Wang, H. Cheng, Y. Liu, Z. Zheng, Coupling benzylamine oxidation with CO_2 photoconversion to ethanol over a black phosphorus and bismuth tungstate S-scheme heterojunction, Angew. Chem. Int. Ed. (2023), e202302919.

[11] W. Liu, Y. Wang, H. Huang, J. Wang, G. He, J. Feng, T. Yu, Z. Li, Z. Zou, Spatial decoupling of redox chemistry for efficient and highly selective amine photoconversion to imines, J. Am. Chem. Soc. 145 (2023) 7181–7189.

[12] P. Wang, S. Fan, X. Li, J. Wang, Z. Liu, Z. Niu, M.O. Tadé, S. Liu, Single Pd atoms synergistically manipulating charge polarization and active sites for

simultaneously photocatalytic hydrogen production and oxidation of benzylamine, Nano Energy 95 (2022), 107045.

[13] D. Sun, Y. Chen, X. Yu, Y. Yin, G. Tian, Engineering high-coordinated cerium single-atom sites on carbon nitride nanosheets for efficient photocatalytic amine oxidation and water splitting into hydrogen, Chem. Eng. J. 462 (2023), 142084.

[14] T. Wang, X. Tao, X. Li, K. Zhang, S. Liu, B. Li, Synergistic Pd single atoms, clusters, and oxygen vacancies on TiO_2 for photocatalytic hydrogen evolution coupled with selective organic oxidation, Small 17 (2021), 2006255.

[15] Z. Tian, C. Han, Y. Zhao, W. Dai, X. Lian, Y. Wang, Y. Zheng, Y. Shi, X. Pan, Z. Huang, H. Li, W. Chen, Efficient photocatalytic hydrogen peroxide generation coupled with selective benzylamine oxidation over defective ZrS_3 nanobelts, Nat. Commun. 12 (2021) 2039.

[16] X. Deng, P. Chen, X. Wang, R. Cui, C. Deng, Dual-vacancy-mediated polarization electric field in $ZnIn_2S_4$ for enhancing photocatalytic hydrogen evolution coupled with selective benzylamine oxidation, Sci. China Mater. 66 (2023) 2299–2307.

[17] Y. Chen, M. Ma, J. Hu, Z. Chen, P. Jiang, L. Amirav, S. Yang, Z. Xing, Coherent nanointerface between light-harvesting and catalytic transition metal sulfides for efficient photochemical conversion, Appl. Catal. B Environ. 324 (2023), 122300.

[18] Y. Liu, W. Yang, Q. Chen, D.A. Cullen, Z. Xie, T. Lian, Pt particle size affects both the charge separation and water reduction efficiencies of CdS–Pt nanorod photocatalysts for light driven H_2 generation, J. Am. Chem. Soc. 144 (2022) 2705–2715.

[19] W. Wang, Y. Tao, J. Fan, Z. Yan, H. Shang, D.L. Phillips, M. Chen, G. Li, Fullerene–graphene acceptor drives ultrafast carrier dynamics for sustainable CdS photocatalytic hydrogen evolution, Adv. Funct. Mater. 32 (2022), 2201357.

[20] L. Cheng, Q. Xiang, Y. Liao, H. Zhang, CdS-based photocatalysts, Energy Environ. Sci. 11 (2018) 1362–1391.

[21] Q. Zhu, Q. Xu, M. Du, X. Zeng, G. Zhong, B. Qiu, J. Zhang, Recent progress of metal sulfide photocatalysts for solar energy conversion, Adv. Mater. 34 (2022), 2202929.

[22] M. Klarner, S. Hammon, S. Feulner, S. Kümmel, L. Kador, R. Kempe, Visible light-driven dehydrogenation of benzylamine under liberation of H_2, ChemCatChem 12 (2020) 4593–4599.

[23] B. Qiu, M. Du, Y. Ma, Q. Zhu, M. Xing, J. Zhang, Integration of redox cocatalysts for artificial photosynthesis, Energy Environ. Sci. 14 (2021) 5260–5288.

[24] H.S. Moon, K.-C. Hsiao, M.-C. Wu, Y. Yun, Y.-J. Hsu, K. Yong, Spatial separation of cocatalysts on Z-scheme organic/inorganic heterostructure hollow spheres for enhanced photocatalytic H_2 evolution and in-depth analysis of the charge-transfer mechanism, Adv. Mater. 35 (2023), 2200172.

[25] H. Zhao, Z. Jiang, K. Xiao, H. Sun, H.S. Chan, T.H. Tsang, S. Yang, P.K. Wong, Photo-assisted separation of noble-metal-free oxidation and reduction cocatalysts for graphitic carbon nitride nanosheets with efficient photocatalytic hydrogen evolution, Appl. Catal. B Environ. 280 (2021), 119456.

[26] Y. Qi, J. Zhang, Y. Kong, Y. Zhao, S. Chen, D. Li, W. Liu, Y. Chen, T. Xie, J. Cui, C. Li, K. Domen, F. Zhang, Unraveling of cocatalysts photodeposited selectively on facets of $BiVO_4$ to boost solar water splitting, Nat. Commun. 13 (2022) 484.

[27] W. Li, Z. Wei, Z. Sheng, J. Xu, Y. Ren, J. Jing, J. Yang, J. Li, Y. Zhu, Dual cocatalysts synergistically promote perylene diimide polymer charge transfer for enhanced photocatalytic water oxidation, ACS Energy Lett. 8 (2023) 2652–2660.

[28] H. Zhao, L. Jian, M. Gong, M. Jing, H. Li, Q. Mao, T. Lu, Y. Guo, R. Ji, W. Chi, Y. Dong, Y. Zhu, Transition-metal-based cocatalysts for photocatalytic water splitting, Small Struct. 3 (2022), 2100229.

[29] D. Gao, J. Xu, L. Wang, B. Zhu, H. Yu, J. Yu, Optimizing atomic hydrogen desorption of sulfur-rich NiS_{1+x} cocatalyst for boosting photocatalytic H_2 evolution, Adv. Mater. 34 (2022), 2108475.

[30] F. Li, J. Chen, Q. Zhang, Y. Wang, Hydrous ruthenium oxide supported on Co_3O_4 as efficient catalyst for aerobic oxidation of amines, Green Chem. 10 (2008) 553–562.

[31] Y. Chen, K. Dong, L. Amirav, Ternary dumbbell nanowires for photocatalytic hydrogen production, Chem. Mater. 34 (2022) 9373–9383.

[32] N. Shi, W. Cheng, H. Zhou, T. Fan, M. Niederberger, Facile synthesis of monodisperse Co_3O_4 quantum dots with efficient oxygen evolution activity, Chem. Commun. 51 (2015) 1338–1340.

[33] D. Gao, J. Xu, L. Wang, B. Zhu, H. Yu, J. Yu, Optimizing atomic hydrogen desorption of sulfur-rich NiS_{1+x} cocatalyst for boosting photocatalytic H_2 evolution, Adv. Mater. 34 (2022), 2108475.

[34] R. Iyengar, D. Sathyanarayana, C. Patel, Thioacetamide complexes of nickel (II) and copper (I) chlorides, J. Inorg. Nucl. Chem. 34 (1972) 1088–1091.

[35] C. Flint, M. Goodgame, Spectral studies of some transition-metal–thioacetamide complexes, J. Chem. Soc. A (1968) 750–752.

[36] H. Yu, R. Yuan, D. Gao, Y. Xu, J. Yu, Ethyl acetate-induced formation of amorphous MoS_x nanoclusters for improved H_2-evolution activity of TiO_2 photocatalyst, Chem. Eng. J. 375 (2019) 121934.

[37] X. Chen, Z. Wang, X. Wang, J. Wan, J. Liu, Y. Qian, A single-source approach to metastable Ni_3S_4 crystallites and their optical properties, Chem. Lett. 33 (2004) 1294–1295.

[38] X. Jia, H. Kang, X. Yang, Y. Li, K. Cui, X. Wu, W. Qin, G. Wu, Amorphous Ni (III)-based sulfides as bifunctional water and urea oxidation anode electrocatalysts for hydrogen generation from urea-containing water, Appl. Catal. B Environ. 312 (2022) 121389.

[39] S.E. Habas, P. Yang, T. Mokari, Selective growth of metal and binary metal tips on CdS nanorods, J. Am. Chem. Soc. 130 (2008) 3294–3295.

[40] T. Mokari, C.G. Sztrum, A. Salant, E. Rabani, U. Banin, Formation of asymmetric one-sided metal-tipped semiconductor nanocrystal dots and rods, Nat. Mater. 4 (2005) 855–863.

[41] K. Khan, X. Tao, Y. Zhao, B. Zeng, M. Shi, N. Ta, J. Li, X. Jin, R. Li, C. Li, Spatial separation of dual-cocatalysts on one-dimensional semiconductors for photocatalytic hydrogen production, J. Mater. Chem. A 7 (2019) 15607–15614.

[42] X. Lu, C.Y. Toe, F. Ji, W. Chen, X. Wen, R.J. Wong, J. Seidel, J. Scott, J.N. Hart, Y. H. Ng, Light-Induced formation of MoO_xS_y clusters on CdS nanorods as cocatalyst for enhanced hydrogen evolution, ACS Appl. Mater. Interfaces 12 (2020) 8324–8332.

[43] K. Dong, Q.-C. Chen, Z. Xing, Y. Chen, Y. Qi, N.G. Pavlpoulos, L. Amirav, Silver tipping of CdSe@CdS nanorods: how to avoid cation exchange, Chem. Mater. 33 (2021) 6394–6402.

[44] Y. Chen, L. Amirav, Shape tunability of copper nanocrystals deposited on nanorods, Chem. Sci. (2023).

[45] C.M. Wolff, P.D. Frischmann, M. Schulze, B.J. Bohn, R. Wein, P. Livadas, M. T. Carlson, F. Jäckel, J. Feldmann, F. Würthner, J.K. Stolarczyk, All-in-one visible-light-driven water splitting by combining nanoparticulate and molecular co-catalysts on CdS nanorods, Nat. Energy 3 (2018) 862–869.

[46] L.J. Hill, M.M. Bull, Y. Sung, A.G. Simmonds, P.T. Dirlam, N.E. Richey, S. E. DeRosa, I.-B. Shim, D. Guin, P.J. Costanzo, N. Pinna, M.-G. Willinger, W. Vogel, K. Char, J. Pyun, Directing the deposition of ferromagnetic cobalt onto Pt-tipped CdSe@CdS nanorods: synthetic and mechanistic insights, ACS Nano 6 (2012) 8632–8645.

[47] K. Zhang, S. Qian, W. Kim, J.K. Kim, X. Sheng, J.Y. Lee, J.H. Park, Double 2-dimensional H_2-evolving catalyst tipped photocatalyst nanowires: a new avenue for high-efficiency solar to H_2 generation, Nano Energy 34 (2017) 481–490.

[48] J. Huang, B. Wang, Z. Hao, Z. Zhou, Y. Qu, Boosting charge separation and broadening NIR light response over defected WO_3 quantum dots coupled g-C_3N_4 nanosheets for photocatalytic degrading antibiotics, Chem. Eng. J. 416 (2021), 129109.

[49] Z. Zhao, Z. Wang, J. Zhang, C. Shao, K. Dai, K. Fan, C. Liang, Interfacial chemical bond and oxygen vacancy-enhanced In_2O_3/CdSe-DETA S-scheme heterojunction for photocatalytic CO_2 conversion, Adv. Funct. Mater. 33 (2023) 2214470.

[50] S. Meng, H. Wu, Y. Cui, X. Zheng, H. Wang, S. Chen, Y. Wang, X. Fu, One-step synthesis of 2D/2D–3D NiS/Zn3In2S6 hierarchical structure toward solar-to-chemical energy transformation of biomass-relevant alcohols, Appl. Catal. B Environ 266 (2020), 118617.

[51] S. Meng, C. Chen, X. Gu, H. Wu, Q. Meng, J. Zhang, S. Chen, X. Fu, D. Liu, W. Lei, Efficient photocatalytic H_2 evolution, CO_2 reduction and N_2 fixation coupled with organic synthesis by cocatalyst and vacancies engineering, Appl. Catal. B Environ. 285 (2021), 119789.

[52] Y. Mao, L. Lin, Y. Chen, M. Yang, L. Zhang, X. Dai, Q. He, Y. Jiang, H. Chen, J. Liao, Preparation of site-specific Z-scheme g-C_3N_4/PAN/PANI@ $LaFeO_3$ cable nanofiber membranes by coaxial electrospinning: enhancing filtration and photocatalysis performance, Chemosphere (2023), 138553.

[53] K. Zhang, J. Ran, B. Zhu, H. Ju, J. Yu, L. Song, S.Z. Qiao, Nanoconfined nickel@ carbon core–shell cocatalyst promoting highly efficient visible-light photocatalytic H_2 production, Small 14 (2018), 1801705.

[54] R. Mazzaro, S.B. Bibi, M. Natali, G. Bergamini, V. Morandi, P. Ceroni, A. Vomiero, Hematite nanostructures: an old material for a new story. Simultaneous photoelectrochemical oxidation of benzylamine and hydrogen production through Ti doping, Nano Energy 61 (2019) 36–46.

[55] A. Agosti, Y. Nakibli, L. Amirav, G. Bergamini, Photosynthetic H_2 generation and organic transformations with CdSe@ CdS-Pt nanorods for highly efficient solar-to-chemical energy conversion, Nano Energy 70 (2020), 104510.

[56] H.S. Moon, K.-C. Hsiao, M.-C. Wu, Y. Yun, Y.-J. Hsu, K. Yong, Spatial separation of cocatalysts on Z-scheme organic/inorganic heterostructure hollow spheres for enhanced photocatalytic H_2 evolution and in-depth analysis of the charge-transfer mechanism, Adv. Mater. 35 (2023), 2200172.

[57] X. Lu, C.Y. Toe, F. Ji, W. Chen, X. Wen, R.J. Wong, J. Seidel, J. Scott, J.N. Hart, Y. H. Ng, Light-induced formation of MoO x S y clusters on CdS nanorods as cocatalyst for enhanced hydrogen evolution, ACS Appl. Mater. Interfaces 12 (2020) 8324–8332.

[58] Z. Xing, Z. Hu, M. Ma, H. Lin, Y. An, Z. Liu, Y. Zhang, J. Li, S. Yang, From one to two: in situ construction of an ultrathin [2]D–[2]D closely bonded heterojunction from a single-phase monolayer nanosheet, J. Am. Chem. Soc. 141 (2019) 19715–19727.

[59] Y. Wang, J. Jin, W. Chu, D. Cahen, T. He, Synergistic effect of charge generation and separation in epitaxially grown $BiOCl$/Bi_2S_3 nano-heterostructure, ACS Appl. Mater. Interfaces 10 (2018) 15304–15313.

[60] Q. Li, X. Ma, H. Liu, Z. Chen, H. Chen, S. Chu, Self-organized growth of two-dimensional GaTe nanosheet on ZnO nanowires for heterojunctional water splitting applications, ACS Appl. Mater. Interfaces 9 (2017) 18836–18844.

[61] Y. Hu, Y. Wu, J. Feng, H. Huang, C. Zhang, Q. Qian, T. Fang, J. Xu, P. Wang, Z. Li, Z. Zou, Rational design of electrocatalysts for simultaneously promoting bulk charge separation and surface charge transfer in solar water splitting photoelectrodes, J. Mater. Chem. A 6 (2018) 2568–2576.

[62] S. Meng, Y. Cui, H. Wang, X. Zheng, X. Fu, S. Chen, Noble metal-free [0]D–[1]D NiS_x/ CdS nanocomposites toward highly efficient photocatalytic contamination removal and hydrogen evolution under visible light, Dalton Trans. 47 (2018) 12671–12683.

[63] O. Yehezkeli, D.R.B. de Oliveira, J.N. Cha, Electrostatically assembled CdS-Co_3O_4 nanostructures for photo-assisted water oxidation and photocatalytic reduction of dye molecules, Small 11 (2015) 668–674.